Biophysical Journal

Article

Biophysical Society

Negative lipid membranes enhance the adsorption of TAT-decorated elastin-like polypeptide micelles

Vivien Walter,[1] Tatiana Schmatko,[1,*] Pierre Muller,[1] André P. Schroder,[2] Sarah R. MacEwan,[3] Ashutosh Chilkoti,[3] and Carlos M. Marques[4,*]

[1]Institut Charles Sadron, CNRS UPR22 & Université de Strasbourg, Strasbourg, France; [2]CNRS, INSA Lyon, LaMCoS, UMR5259, Villeurbanne, France; [3]Department of Biomedical Engineering, Duke University, Durham, North Carolina; and [4]University of Lyon, ENS-Lyon, CNRS UMR 5182, Chem. Lab, Lyon, France

ABSTRACT   A cell-penetrating peptide (CPP) is a short amino-acid sequence capable of efficiently translocating across the cellular membrane of mammalian cells. However, the potential of CPPs as a delivery vector is hampered by the strong reduction of its translocation efficiency when it bears an attached molecular cargo. To overcome this problem, we used previously developed diblock copolymers of elastin-like polypeptides (ELP$_{BC}$s), which we end functionalized with TAT (transactivator of transcription), an archetypal CPP built from a positively charged amino acid sequence of the HIV-1 virus. These ELP$_{BC}$s self-assemble into micelles at a specific temperature and present the TAT peptide on their corona. These micelles can recover the lost membrane affinity of TAT and can trigger interactions with the membrane despite the presence of a molecular cargo. Herein, we study the influence of membrane surface charge on the adsorption of TAT-functionalized ELP micelles onto giant unilamellar vesicles (GUVs). We show that the TAT-ELP$_{BC}$ micelles show an increased binding constant toward negatively charged membranes compared to neutral membranes, but no translocation is observed. The affinity of the TAT-ELP$_{BC}$ micelles for the GUVs displays a stepwise dependence on the lipid charge of the GUV, which, to our knowledge, has not been reported previously for interactions between peptides and lipid membranes. By unveiling the key steps controlling the interaction of an archetypal CPP with lipid membranes, through regulation of the charge of the lipid bilayer, our results pave the way for a better design of delivery vectors based on CPPs.

SIGNIFICANCE   TAT is a short amino acid sequence that interacts efficiently with cellular membranes. Although the affinity of a single TAT for the membrane is hampered when it is attached to a cargo molecule, assembly into micelles of TAT-decorated diblock copolymers allows recovering the lost affinity. Here, we study how lipid membrane charges can tune the interactions of such micelles by means of confocal fluorescence microscopy on giant unilamellar vesicles. We quantitatively determine the micellar binding constants as a function of membrane charge, revealing a sigmoidal dependence not seen before in the context of peptide-biomembrane interactions. Our work paves the way for better design of peptide sequences promoting cargo-membrane affinity.

INTRODUCTION

Cell-penetrating peptides (CPPs) were discovered in the early 1980s, along with the transactivator of transcription (TAT) domain of the HIV-1 virus (1,2). Other CPPs were

discovered later, such as penetratin from the drosophila antennapedia HOX gene (3) or transportan (4). More specifically for TAT, the purely cationic sequence, from amino acid 47 to 57, was found to be responsible for the translocation of the viral particles into the infected cell. Currently, TAT and other CPP sequences are mainly used as drug delivery vectors (5). Several translocation mechanisms have been proposed (6,7), including active and nonactive pathways (8–10). To better assess the translocation efficiency of TAT, in the absence of active, energy-driven processes, studies have been performed in lipid bilayer models (11–13). One usually takes cell penetrating as a synonym for membrane penetrating, but many of the CPPs (including TATs) do not passively cross membranes, as we are

describing below, unless nonphysiological molar fractions of 1,2-dioleoyl-sn-glycero-phosphoetanolamine (DOPE), a lipid with an inverted conical shape that induces a negative spontaneous curvature of the lipid leaflets, are added. On giant unilamellar vesicles (GUVs) made of ternary mixtures of 1,2-dioleoyl-sn-glycero-phosphocholine (DOPC), 1,2-dipalmytoyl-sn-glycero-3-phosphocholine, and cholesterol, Ciobanasu et al. showed that TAT binding to the surface of GUVs induces the leakage of small dyes but without CPP translocation (14).The inclusion of a small proportion of negatively charged lipids in the membrane composition increased the affinity of TAT for the membrane but did not promote translocation. They concluded from these experiments that pores of nanometric size are formed. The same authors also found that TATs have a higher mobility than the membrane lipids with which they interact (15). They proposed that CPPs float above the lipid membrane, although a fast diffusion coefficient suggests that CPPs may increase the fluidity of membranes they interact with. Indeed, Akabori et al. (16) have since found by SAXS (small-angle X-ray scattering) experiments on oriented multilayers that once TAT is bound to the membrane, the average area per lipid head is increased along with a decrease of the membrane bending modulus. On neutral membranes, SAXS electron density profiles show that TAT peptides, despite their cationic nature, are inserted close to the aliphatic chains such that they bind to and drag along the lipid phosphate groups. The incorporation of anionic lipids in the supported bilayer keeps TAT peptides further away from the aliphatic chains, likely due to the stronger affinity for the charged head groups. Wong and co-workers have shown that TAT penetrates GUVs only when the lipid composition contains DOPE. They also performed SAXS experiments on liposomes exposed to TAT and show that, upon exposure to TAT, the lipid undergoes a drastic structural change from a lamellar phase to a cubic double-diamond phase (17,18). More recently, Allolio and co-workers have shown that GUVs self-assembled from a ternary mixture of DOPC/1,2-dioleoyl-sn-glycero-3-phospho-(1′-rac-glycerol) (DOPG)/DOPE leak small dyes and fuse when exposed to TAT. Transmission electron microscopy experiments performed on liposomes by the same authors have shown that the fusion is associated with the multilamellar structure of the liposomes. With the help of molecular dynamic simulations, the authors proposed a membrane fusion model based on pore formation (19). Along the same line, Sakamoto et al. have shown that osmotic pressure shocks or chaotropic solutes could also induce curvature changes in an egg-phosphatidylcholine (PC) membrane and promote CPP entry (20).

We have recently designed a family of temperature-responsive diblock copolymers made of elastin-like polypeptides (ELP$_{BC}$s). Above a critical micellar temperature (CMT), the solvent becomes a poor solvent for one of the blocks, forcing the ELP$_{BC}$ to self-assemble into spherical micelles, as confirmed by static and dynamic light scattering experiments and by small-angle neutron scattering (21). In the present work, ELP$_{BC}$s have been end functionalized with a TAT sequence on one end and tagged with a fluorophore on the other end. Above the CMT, the fluorescent dye (leader), which is covalently grafted to the N-terminus of the hydrophobic block, remains in the core of the micelle, while the TAT moieties (trailers) grafted to the C-terminus of the hydrophilic block are dangling out on the corona of the micelle. Due to the length of the polypeptide chain, we can consider ELP$_{BC}$ as a model of a cargo that is carried into the cell by TAT; a real drug delivery system would include a drug in place of the fluorophore. The presence of a cargo usually reduces the translocation efficiency of TAT (22,23); nevertheless, the ELP$_{BC}$s assembled in micelles have proven to be very efficient in crossing the membrane barrier of several lines of cancer cells (24), especially when decorated with a CPP containing six or more arginine residues. In particular, the TAT sequence contains six arginines and two lysines. A major advantage of using such a micellar system instead of liposomes, for instance, is that because their CMT can be tuned by design of the hydrophobic block, the micellization that is accompanied by an increase of affinity can be specifically used to target locations in the body where there is hyperthermia (25). Experiments performed in cancer cells by other groups as well have shown that ELP micelles are internalized without disruption upon crossing. The fluorescence of the ELPs is clearly seen as dots accumulating inside the cells rather than as broad fluorescence everywhere in the cytoplasm. Although ELP-micelle fluorescence is large on the cell membrane, colocalization with lysosome markers is observed (26). Our study on model membranes was meant to understand the basis of the interactions between this class of molecules and cells.

We have previously reported that the self-assembly of ELP$_{BC}$s into micelles recovers the affinity of the TAT peptides for model lipid membranes (27). Hence, the unimeric forms of TAT-ELP$_{BC}$s do not display any adsorption on neutral membranes, whereas TAT-ELP$_{BC}$s micelles show significant adsorption without losing their micellar structure. However, we have not witnessed any penetration in these model systems. This is an indication that the translocation mechanism seen for living cells can probably be decomposed in two different steps, a first one that would be driven mostly by electrostatic interactions and a second one that requires the machinery of the cell.

In this article, we quantitatively study the effect of an increase in lipid membrane charge density on the adsorption behavior of TAT-functionalized ELP unimers and micelles. By measuring adsorption amounts for a range of TAT-ELP$_{BC}$ bulk concentrations and for surface molar charges between 0% and 20%, we extract affinity constants and compare our results with those obtained for cargo-less TAT sequences. We also study the effect of temperature

on the adsorption amounts and witness a drastic increase of TAT-ELP$_{BC}$ binding as the temperature rises.

MATERIALS AND METHODS

Materials

The phospholipids used in this work, namely DOPC and DOPG were purchased from Avanti Polar Lipids (Alabaster, AL, USA) already dissolved in chloroform and stored at $-18°C$. Chloroform, acetone, and ethanol for cleaning purposes were purchased from Carlo Erba Reagents (Milan, Italy). Other reagents, such as glucose, sucrose, and PBS tablets were obtained from Sigma-Aldrich (Burlington, MA, USA) and used without further purification unless specified in the text. The CPPs used in this work are TAT$_{47-57}$ terminated elastin-like block copolymer polypeptides (TAT-ELP$_{BC}$ and TAT-ELP$_{BC}$-Alexa Fluor 488). Their synthesis has been reported in ref. (24). The ELP$_{BC}$ consists of two different blocks of 60 pentapeptides of Val-Pro-Gly-Xaa-Gly (VPGXG) derived from native tropoelastin where X is a guest residue, being any amino acid except proline. ELPs exhibit lower critical solution temperature phase separation behavior in aqueous solvents, wherein a solution of an ELP will phase separate above a critical cloud point temperature into an ELP-rich dense phase and an ELP-depleted dilute phase. The phase diagram of an ELP can be tuned by its composition (X residues in the Val-Pro-Gly-Xaa-Gly repeat) and its chain length (28,29). In the hydrophobic block of the ELP$_{BC}$ used herein, Xaa is Val. In the hydrophilic block, Xaa is Gly and Ala with a 1:1 ratio. For some diblocks, a maleimide derivative of the Alexa Fluor 488 fluorescent dye (Molecular Probes, Eugene, OR, USA) was covalently conjugated to the end of the hydrophobic block at a terminal cysteine residue (see Fig. 1 for a schematic depiction of the ELP$_{BC}$). The ELP$_{BC}$s were dissolved in PBS (ready-to-use tablets from Sigma-Aldrich) at the desired concentrations. To prepare fluorescently labeled ELP$_{BC}$ solutions for microscopy, unlabeled ELP$_{BC}$s were mixed with Alexa Fluor 488-labeled ELP$_{BC}$s at a 100:1 ratio in order to avoid any quenching of the fluorescence. At their CMT ($32°C$), these polypeptides self-assemble into micelles with the TAT sequences exposed at the corona of the micelle and the fluorescent marker trapped inside the core. The ELP$_{BC}$ solutions and their fluorescent versions were aliquoted and stored at $-18°C$. Before each experiment, one aliquot (500 μL, 25 μM) was thawed overnight at $4°C$ under constant agitation and then centrifuged for 1 min at $22,500 \times g$ at $4°C$.
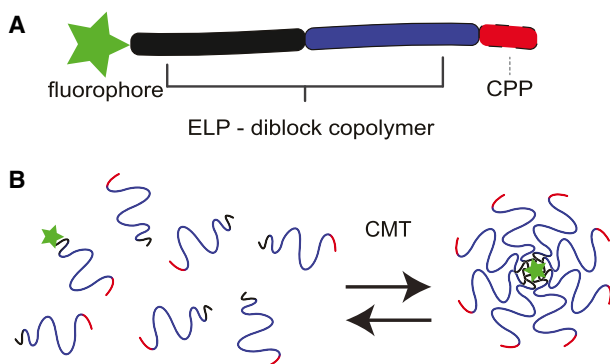

FIGURE 1 (A) Schematic representation of the ELP$_{BC}$. The hydrophobic block (in *black*) is composed of 60 repeats of VPGVG. A small fraction is functionalized with an Alexa Fluor 488 fluorescent dye (in *green*). The hydrophilic block (in *blue*) is composed of 60 repeats of the Val-Pro-Gly-Xaa-Gly, where X is G or A in a 1:1 ratio. This block is fused to the CPP sequence TAT$_{47-57}$ (in *red*) at its C-terminus. (B) Sketch of the self-assembly of ELP$_{BC}$ into micelles (of roughly 20 nm radius of gyration) above the CMT. To see this figure in color, go online.

Preparation of GUVs

Giant vesicles were obtained by the electroformation technique (30). Sucrose and glucose were dissolved in milliQ water (Millipore, Burlington, MA, USA), the solution osmolarity was measured with an osmometer (Osmomat 030, Gonotec, Berlin, Germany) and adjusted to 280 mOsm.L^{-1}, then filtered with a syringe with a 0.2 μm mesh size filter. Syringes were mounted with a new sterile filter unit to be stored at $4°C$. Once prepared, sugar solutions were used within a week. 5 μL of a lipid solution at 1 mg mL^{-1} in chloroform (high-performance liquid chromatography [HPLC] grade) was deposited on each electrode of a homemade electroformation chamber. A moderate vacuum was applied to evaporate chloroform in order to obtain lipid stacks. The electroformation chamber was then filled with 1 mL sucrose and closed. An oscillatory electric field was applied across the chamber for 4–15 h at room temperature. Its amplitude and frequency were set, respectively, to 1 V peak to peak and 10 Hz. The obtained GUVs were diluted with 1 mL iso-osmotic glucose and left to settle down for 15–30 min before use.

Chamber coating and sample preparation for microscopy imaging

To avoid GUV adhesion on glass, microscope slides were functionalized with polyethylene glycol (PEG) with a molecular weight of 5000 Da using a variation of the protocol described by Perret et al. (31). Glass slides were washed with chloroform, acetone, and ethanol successively and dried under a nitrogen flow. The silanol groups at the glass surface were then activated by UV-ozone cleaning (Novascan Technologies, Ames, IA, USA) for approximatively 1 h in total for both sides. Silanization was performed at room temperature in a mixture of 99.7% HPLC-grade ethanol, 0.2% ultrapure water (Milli-Q systems by Millipore), and 0.1% mercaptopropyl triethoxy silane (MPTS). To control the water concentration necessary for gentle silane hydrolysis at the surface, special precautions were taken: before each experiment, MPTS was freshly distilled under vacuum, and a new sealed bottle of ethanol (HPLC grade) was used, as high water amounts would give rise to 3D bulk polymerization of the silane. Clean slides were immersed in the silanization solution for 1 h under argon atmosphere and then rinsed twice in fresh ethanol. After drying under nitrogen, slides were cured in an oven at $110°C$ for 10 min to enhance covalent bonding. They were sonicated for 30 s again in ethanol to remove physisorbed MPTS. Then, they were dried under flowing nitrogen and placed in a sandwich-like configuration in contact with 25 μL of a Mal-PEG$_{5000}$-methoxy of 140 μM PBS (pH 6.5) for at least 24 h. The above environment was kept saturated with water to prevent evaporation. Sandwiches were opened just before use; slides were rinsed extensively with milliQ water, sonicated for 30 s, and dried under flowing nitrogen.

The microscopy observation cell was made of two circular PEGylated slides (as described above) separated by a ring-like inox spacer. A thin layer of grease (Apiezon, Jefferson Hills, PA, USA) was used to seal the bottom slide to avoid leakage. 80 μL of the GUVs in a 1:1 glucose/sucrose solution was pipetted and put in the observation chamber that contained 320 μL of a 25 μM solution of the ELP$_{BC}$ in PBS buffer at 280 mOsm.L^{-1}, leading to a final concentration of 20 μM in PBS/glucose/sucrose. The observation chamber was closed and heated to the desired temperature for 90 min before starting the microscopy experiments. We used a homemade heating plate and a heating objective mantel (ALA Scientific, Farmingdale, NY, USA) to precisely control the temperature.

Confocal microscopy and image processing

Fluorescence imaging was performed using confocal laser scanning microscopy. An inverted TE-2000 microscope (Nikon, Tokyo, Japan) equipped with a $60\times$ WI/1.2NA Plan Apo DIC objective and a Nikon C1 scan head was used in our experiments. Images were captured using EZ-C1 software (Nikon, v.3.50). Alexa Fluor 488-labeled TAT-ELP$_{BC}$s were excited using an argon-ion laser (Melles-Griot, Rochester, NY, USA) at 488 nm.

Quantitative fluorescence intensity analysis was performed on the confocal images using the "Radial Profile Extended" plug-in from ImageJ. Briefly, for each GUV, we plotted its averaged radial intensity profile, from which we extracted the excess of fluorescence on the membrane due to peptide adsorption, as described previously (27).

In the range of concentrations for which fluorescence intensity is proportional to the number of fluorescent species per unit volume, we calculate absolute local concentrations using the bulk peptide concentration C_b. Hence, as the Fig. 2 A shows, an empty GUV immersed in a solution of fluorescent peptides that adsorb on the membrane appears as a black disk with a bright corona surrounded by a homogeneous bulk fluorescent background. A sketch of the experiment is depicted in Fig. 2 B. The obtained radial profile (Fig. 2 C) can be fitted by a Gaussian curve added to a sigmoid as one can see in Fig. 2 D, an enlarged view of Fig. 2 C. For each radial coordinate r, we subtracted the sigmoid intensity I_s from the total radial intensity I_r and integrate it over r. The obtained value is normalized with the bulk intensity $I_{b,\infty}$ and the mean radius R of the vesicle. The result of this computation is the number of peptides adsorbed per unit of membrane surface, which, assuming a lipid surface in a bilayer $A_H = 0.65$ nm^2 (32), can be converted to the number of peptides adsorbed per thousand lipids (N_{PTL}) as follows:

$$N_{PTL} = 1000 A_H \frac{C_b}{R.I_{b,\infty}} \int_0^{2\pi} d\theta \int_0^\infty r dr(I_r(r) - I_s(r)) \quad (1)$$

RESULTS

Adsorption as a function of bulk concentration and surface charge

Adsorption of TAT-ELP$_{BC}$s on GUVs with various charge fractions X_q of DOPG in DOPC was investigated as a func-
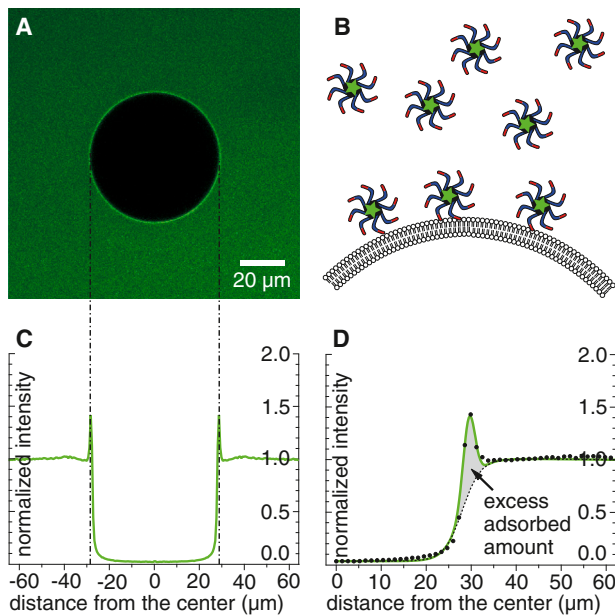
FIGURE 2 (A) Typical confocal laser scanning microscopy image of a GUV immersed in a solution of TAT-ELP$_{BC}$s interacting with the membrane. (B) TAT-ELP$_{BC}$s adsorb on the membrane as micelles as depicted on the sketch. (C) The radial intensity profile can be fitted by a Gaussian function added to a sigmoid. (D) The gray area corresponds to $r dr(I_r(r) - I_s(r))$, i.e., the number of CPP-ELP$_{BC}$s adsorbed per unit of membrane surface. To see this figure in color, go online.

tion of the TAT-ELP$_{BC}$ concentration (C_b). Experiments were performed at 35°C, a temperature at which TAT-ELP$_{BC}$S not only form micelles in bulk but also keep their micellar structure upon adsorption onto the membrane (27). GUVs remained stable over the time of the experiments for the range of concentrations, compositions, and temperatures that we explored.

Adsorption of TAT-ELP$_{BC}$S on GUVs is presented as a surface plot on Fig. 3 A, where N_m, the number of adsorbed micelles per thousand lipids, is shown as a function of C_m, the micellar concentration, and X_q, the fraction of charged lipids in the membrane. Each value of N_m is an average over at least 30 GUVs. Five membrane compositions $X_q = 0\%$, 5%, 10%, 15%, and 20%, and several bulk concentrations C_b ranging from 7.5 to 60 μM were explored, corresponding to a micelle concentration range $C_m \approx$ 100–800 nM. C_m is calculated as $C_m = C_b/p$, with $p = 73$ the micelle aggregation number at 35°C (21). For each prescribed charge fraction X_q, the adsorbed amount of micelles N_m as a function of micelle bulk concentration C_m is well described by the Langmuir isotherm (33):

$$N_m = N_m^{max} \frac{K_m C_m}{1 + K_m C_m} \quad (2)$$

where N_m^{max} expresses the maximum value of adsorbed micelles per thousand lipids and K_m is the adsorption constant of TAT-ELP$_{BC}$ micelles, which depends on X_q.

Dependence of N_m on membrane charge X_q is shown as a 2D plot in Fig. 3 B for the three micelle bulk concentrations $C_m = 0.14$, 0.27, and 0.62 μM. They all show a similar tendency, i.e., a sigmoidal increase of N_m with X_q around some characteristic charge fraction X_q^0. Hence, the whole set of data has been fitted to the Langmuir adsorption isotherm in Eq. 3 with a sigmoidal empirical form for the X_q dependence of K_m:

$$K_m(X_q) = K_m^0 \left(1 + \frac{J - 1}{1 + \exp\left(- \frac{X_q - X_q^0}{\Delta X_q} \right)} \right), \quad (3)$$

where K_m^0 is the adsorption constant of TAT-ELP$_{BC}$ micelles on a neutral membrane X_q^0 is the charge fraction threshold. J and ΔX_q are, respectively, the numerical factors describing the amplitude and the width of the empirical function.

The surface plot in Fig. 3 A, which represents the best fit to the data using Eqs. 2 and 3, is obtained for the set of values $N_m^{max} = 0.78$, $K_m^0 = 1.1 \times 10^6$ M^{-1}, $X_q^0 = 7\%$, $J = 2.2$, and $\Delta X_q = 1.5\%$. Continuous lines in Fig. 3, A– C, correspond to this best fit.

The existence of the two distinct charge regimes, implicitly assumed by the choice of the sigmoidal Eq. 3, is better shown in Fig. 3 C by the Langmuir isotherms that have been separated into a low-charge group ($X_q \leq X_q^0 = 7\%$) (blue symbols), and a
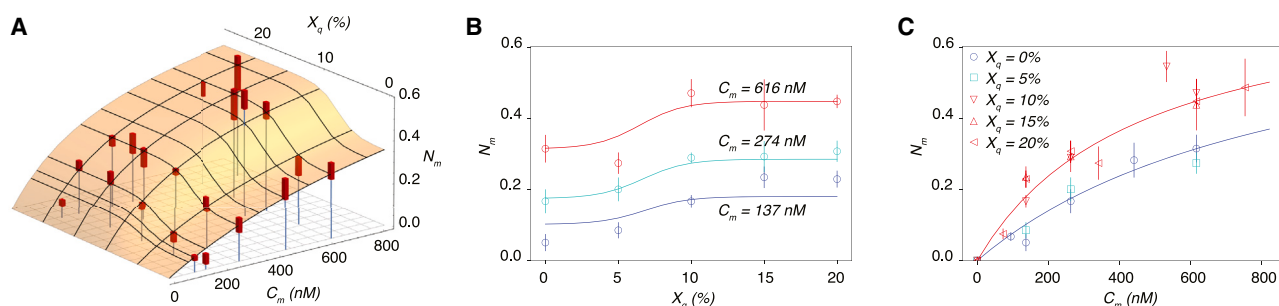
FIGURE 3 TAT-ELP$_{BC}$ adsorption on GUVs made of various DOPG/DOPC compositions. $C_m = C_b/p$ is for bulk molar concentrations of TAT-ELP$_{BC}$ micelles with aggregation number p, and X_q is for DOPG molar fraction. (*A*) 3D representation of the data with a surface plot corresponding to the best fit obtained as explained in the text. (*B*) 2D representation of the data as a function of X_q only for three different values of the micelle concentration C_m. Same best fit as in (*A*), represented by full lines. (*C*) 2D representation of the data as a function of C_m only for five different values of the charge fraction X_q. Same best fit as in (*A*), represented by full lines for the low- (in *blue*) and high-charge (in *red*) fractions ($X_q \leq 5\%$ and $X_q \geq 10\%$). Error bars correspond to the measured statistical distribution of N$_m$ in the sample. To see this figure in color, go online.

high-charge group ($X_q \geq X_q^0$) (*red symbols*). The charge on the membrane (above X_q^0) roughly doubles the value of the binding constant K_m, which varies from $K_m^0 = 1.1 \times 10^6$ M^{-1} for $X_q \leq X_q^0$ to $K_m^0 = 2.4 \times 10^6$ M^{-1} for $X_q \geq X_q^0$. Affinity constants of short TAT moieties (referred hereafter as K) interacting with the surface of liposomes have been measured in the literature by several groups on bilayers assembled from lipids with similar headgroups, PC, and phosphatidylglycerol (PG), albeit with different lipid tails. For neutral membranes, Rao et al. (13) obtained a value of $K = 3.1 \times 10^3$ M^{-1}. For charged membranes, Ziegler and co-workers (34) obtained $K = 6 \times 10^4$ M^{-1} on 20% charged lipids, and Rao et al. reported $K = 1.3 \times 10^5$ M^{-1} with 100% charged lipids. Hence, K_m is greater than K, especially on neutral membranes, reflecting a higher adsorption affinity of TAT-ELP$_{BC}$ micelles to membranes of any charge density compared to TAT without cargos. The K_m of micelles ranges from 10- to 1000-fold that of short chains for charged and neutral membranes, respectively. Note, however, that bulk molar concentrations (C_b) of TAT moieties in micellar solutions are ~70-fold greater than those of micelles. Thus, half-adsorption isotherms for TAT-ELP$_{BC}$s are reached for C_b values ranging between 7- and 0.07-fold of those corresponding to short-chain adsorption.

Considering a molar mass M$_w$ = 49.6 kDa for TAT-ELP$_{BC}$ and an average area per lipid A$_H$ = 0.65 nm^2, $N_m^{max} = 0.78$ corresponds to a mass coverage of 7.2 mg m^{-2}, larger than typical values of adsorbed polymer monolayers ($\simeq 1$ mg.m^{-2}) but consistent with the adsorption of copolymer micellar assemblies. This leads to a mean distance between micelles in close contact of $d_{mic} \simeq 32$ nm, which needs to be compared to their diameter, $d = 40$ nm, taking twice the gyration radius $R_g = 20$ nm at 35°C (21). Hence, the measured N_m^{max} value corresponds to a surface density of TAT-ELP$_{BC}$s on the membrane 1.5 times larger than the one from the compact packing of hard spheres. This suggests that at high C_b, TAT-ELP$_{BC}$ micelles adsorb on the membrane with a quite high degree of interpenetration, as sketched in Fig. 4.

Adsorption as a function of temperature

Adsorption on neutral and on 20% charged membranes has also been studied as a function of the temperature, from 25°C to 42°C, for a fixed bulk peptide concentration $C_b = 20$ μM. The results are displayed in Fig. 5. At temperatures above the CMT, adsorption of TAT-ELP$_{BC}$s is triggered by self-assembly and is significantly increased by raising the temperature even further.

The formation of ELP$_{BC}$ micelles is a complex phenomenon that has been studied in detail by Garanger et al. (21). Their experiments show that the micelle aggregation number
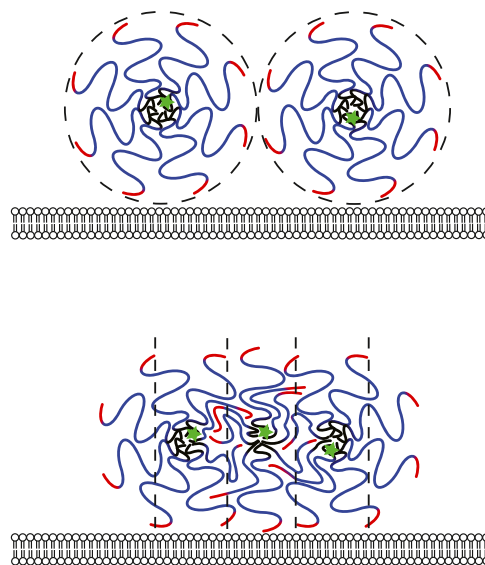

FIGURE 4 Sketch of TAT-ELP$_{BC}$ micelle adsorption scenarios. If micelles are in close contact (*top*), the resulting micelle-micelle distance is $d = 40$ nm. Such a scenario gives a maximum amount of absorbed micelles N_m^{max} smaller than the $N_m^{max} = 0.78$ measured. The latter leads to a micelle-micelle distance $d = 32$ nm corresponding to an increase of the surface density of a factor 1.5. This suggests a quite high interpenetration of micelles (*bottom*). To see this figure in color, go online.
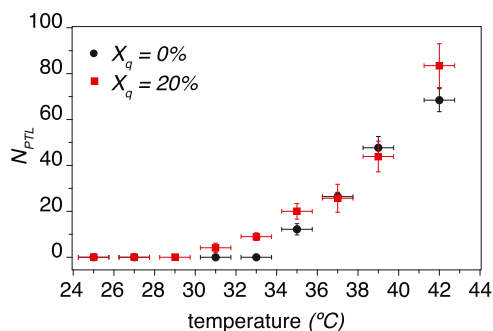
FIGURE 5 N_{PTL} as a function of the temperature for a neutral membrane ($X_q = 0\%$) and a charged membrane $X_q = 20\%$ at bulk concentration $C_b = 20\ \mu M$. The TAT-ELP$_{BC}$ CMT is at 32°C ± 1°C as measured by optical density. Errors bars correspond to ± 1°C and to the measured statistical distribution of N$_{PTL}$ in the sample. To see this figure in color, go online.

p increases gradually from 73 at 35°C to 127 at 45°C. Micellization of TAT-ELP$_{BC}$ is well described by a model developed by Hassouneh et al. (35). The model refers to micellization in these systems as weak micellization due to the low interfacial tension at the surface of a hydrophobic core that retains a significant amount of solvent. As the temperature increases, the core further collapses, expelling solvent, thus increasing the interfacial tension between the core and corona blocks. This results in an increasing aggregation number as the temperature increases above the CMT and changes the micelle core and corona sizes. From the point of view of adsorption of the micelles on lipid membranes in this paper, this implies that a direct comparison of adsorption isotherms at different temperatures is a complex task, as the adsorbing units—the micelles—are different objects at different temperatures; they have different aggregation number, sizes, and presumably also different affinities to the membrane surface.

Despite the underlying variation of the structure of the ELP$_{BC}$ micelles with temperature, several important trends can be observed in Fig. 5. As the figure clearly shows, there is no adsorption below 31°C. For neutral membranes, there is no adsorption up to 33°C; at higher temperatures, the N_{PTL} value increases almost linearly with T. For the 20% charged membranes, the onset of adsorption is at 31°C, followed by an increase with temperature similar to the variation of adsorption on neutral membranes. Micelle adsorption affinities to phospholipid membranes appear therefore to be, in general, enhanced by the presence of charges on the membranes. A precise measurement of such affinities would require the determination of the adsorption isotherms for each of the studied temperatures, a significant undertaking that is well beyond the scope of this work.

DISCUSSION

We have measured the affinity of TAT-ELP$_{BC}$s acting as TAT-coupled cargo molecules on model membranes at physiological charge densities. Below the CMT of the ELP$_{BC}$, the affinity of the TAT-ELP$_{BC}$ unimers for the membrane is suppressed by the presence of the attached cargo, but above the CMT, the micelle structure provides a larger collective multivalent charge density with greater affinity for the lipid bilayer, restoring the ability of the peptide to adsorb on the lipid bilayer. Increasing the membrane charge density by modulating the composition of charged lipids leads, as expected, to an increased affinity for the ELP$_{BC}$ micelles. Interestingly, the functional dependence of the affinity with lipid charge displays a step shape, which, to our knowledge, has not been reported before for the interaction between polymer and lipid membranes.

Such a shape, which corresponds to the existence of two adsorption regimes separated by a crossover membrane charge fraction $X_q^0 = 7\%$, independent of micelle concentration, is indicative of a Bragg-Williams adsorption process of the charged lipids on micelle surface exposed to contact with the membrane (33). Complementary to the simple Langmuir isotherms describing the adsorption to the surface of ideal particles dispersed in bulk due to particle-surface affinity, Bragg-Williams adsorption accounts also for repulsive interactions between the adsorbed particles. For large enough repulsions, there are two adsorption regimes. The first occurs at low bulk concentrations, when the amount of particles on the surface is vanishingly small. The second state, above a crossover concentration that depends on the microscopic description of the repulsions, corresponds to a surface saturated by adsorbed particles. The transition between these two states is first order for large enough repulsions. Below, we transpose the Bragg-Williams description to adsorption as a function of the surface charge instead of bulk concentration. In our case, if we identify the membrane as a 2D reservoir of negatively charged lipids, with attractive interactions to the oppositely charged micelles sitting on the membrane and repulsive interactions between lipids, then the lower-charge regime would correspond to micelles with (almost) no adsorbed charged lipids and the high-charge regime to micelles that have collected (adsorbed) as much charged lipids as they can (saturation). For the lower-charge regime, micelles will have to recruit oppositely charged lipids outside of the adsorbed area, as is extensively described in the literature for proteins embedded in membranes (36). In such cases, anionic lipids will rapidly diffuse toward the positively charged objects. This usually leads to local lipid phase separation in the membrane. In the high-charge regime, a sufficient amount of oppositely charged lipids is already present under the micelle. The plausibility that such a mechanism controls adsorption of TAT-ELP$_{BC}$ micelles on charged membranes surfaces is reinforced by the measured X_q^0 value. Indeed, from a micelle gyration radius $R_g = 20$ nm, from an aggregation number of 73 at 35°C (21), and considering eight charges per peptide (six arginines and two lysines), one finds that each micelle of TAT-ELP$_{BC}$ has a positive surface charge density of the order of 0.1 elementary charges (e) per nm^2. Perhaps unsurprisingly, one finds that a negative charge density

matching these conditions is reached at the inflection of the sigmoidal curve, when the membranes contain a charged lipid fraction $X_q^0 = 7\%$. Refinements of this picture, for instance, considering other values of the micelle radius, different partial ionization degrees for the charged micelles and membrane, or charge screening or membrane wrapping, can change the precise values without compromising the description.

Adsorption of ELPs as micelles appears to be a mostly reversible phenomenon with temperature, as indicated by the almost full loss of membrane fluorescence when the sample is cooled down below the CMT (37). Also, although reversibility with concentration was not specifically addressed in our experiments, the Langmuir isotherm shape of the adsorption curves suggests that adsorption results from the standard equilibrium between bulk and surface, which requires reversibility.

Our measurements of adsorbed amounts as a function of temperature bring new information to a field where the adsorption from micellar solutions of nonionic and ionic surfactants to the air-water and solid-water interfaces has been extensively studied. At the air-water interface, standard adsorption from nonionic surfactant solutions occurs by monomer adsorption, even above the CMC, and displays a larger affinity and surface coverage as the temperature is increased (38). Also, at the air-water interface, monomeric adsorption from ionic surfactant solutions displays increased affinities with temperature but decreasing surfactant densities (39). Our data, which cut through the general Langmuir adsorption diagram (N_m, C_m, T) at a constant monomer concentration—and potentially at nonconstant micellar concentration C_m—display features compatible with increased adsorption affinities at the air-water interface. This is in contrast to the behavior of CTAB surfactant micelles (N,N,N-Trimethylhexadecan-1-aminium bromide) at the solid-liquid interface, where the loss of affinity of the micelles with temperature is reported (40) and where adsorption from micellar solutions implies often a strong reorganization of the structure of the aggregates, even for polymeric surfactants (41). The case of the lipid bilayer interface appears thus as an interesting situation intermediate between the air-water and solid-water interfaces, where affinity can be gained by raising the temperature—related in all cases to lower critical micellar concentrations—but where micellar integrity can be preserved.

CONCLUSION

We have measured the affinity of TAT-ELPBC acting as TAT-coupled cargo molecules on model membranes of physiological charge densities. Below the CMT, the affinity for the membrane is suppressed by the presence of the cargo, but above the CMT, the micellar structure enhances this affinity, restoring the adsorption ability of the peptide. The membrane charge increases slightly the affinity in a step like manner consistent with a Bragg-Williams adsorption mechanism. Experiments performed from 35°C to 42°C show that the adsorption is enhanced upon temperature increase, which we attribute to the accompanied structural change of the micelle.

AUTHOR CONTRIBUTIONS

Experiments were designed by C.M.M., V.W., and T.S. The experiments shown in this work were performed by V.W. and analyzed and interpreted by V.W., T.S., A.P.S., P.M., and C.M.M. The ELP$_{BC}$s used in in this work were designed and synthesized by A.C. and S.R.M. C.M.M., V.W., and T.S. wrote the manuscript. All authors reviewed and corrected the manuscript.

DECLARATION OF INTERESTS

The authors declare no competing interests.

REFERENCES

1. Frankel, A. D., and C. O. Pabo. 1988. Cellular uptake of the TAT protein from human immunodeficiency virus. *Cell.* 55:1189–1193.

2. Green, M., and P. M. Loewenstein. 1988. Autonomous functional domains of chemically synthesized human immunodeficiency virus TAT trans-activator protein. *Cell.* 55:1179–1188.

3. Derossi, D., A. H. Joliot, …, A. Prochiantz. 1994. The third helix of the Antennapedia homeodomain translocates through biological membranes. *J. Biol. Chem.* 269:10444–10450.

4. Pooga, M., M. Hällbrink, …, Ü. Langel. 1998. Cell penetration by transportan. *Faseb. J.* 12:67–77.

5. Torchelin, V. P. 2008. Tat Peptide-mediated intracellular delivery of pharmaceutical nanocarriers. *Adv. Drug Deliv. Rev.* 60:548–558.

6. Richard, J. P., K. Melikov, …, B. Lebleu. 2002. Cell-pentrating Peptides A reevaluation of the mechanism of cellular uptake. *J. Biol. Chem.* 278:585–590.

7. Madani, F., S. Lindberg, …, A. Graslund. 2011. Mechanisms of Cellular Uptake of Cell-Penetrating Peptides. *J. Biophys.* 2011:414729.

8. Bechara, C., and S. Sagan. 2013. Cell-penetrating peptides: 20 years later, where do we stand? *FEBS Lett.* 587:1693–1702.

9. Ter-Avetisyan, G., G. Tünnemann, …, M. C. Cardoso. 2009. Cell Entry of Arginine-rich Peptides is Independent of Endocytosis. *J. Biol. Chem.* 284:3370–3378.

10. Lu, C. Y., J. Y. Huang, and L.-W. Lo. 2017. Depicting Binding-Mediated Translocation of HIV-1 TAT Peptides in living cells with Nanoscale Pens of TAT-conjugated Quantum dots. *Sensors.* 17:315.

11. Ziegler, A., X. L. Blatter, …, J. Seelig. 2003. Protein Transduction Domains of HIV-1 and SIV TAT Interact with Charged Lipid Vesicles. Binding Mechanism and Thermodynamic Analysis. *Biochemistry.* 42:9185–9194.

12. Ziegler, A. 2008. Thermodynamic studies and binding mechanisms of cell penetrating peptides with lipids and glycosaminoglycans. *Adv. Drug Deliv. Rev.* 60:580–597.

Walter et al.

13. Rao, Y., S. J. J. Kwok, …, K. B. Eisenthal. 2014. Label-free probe of HIV-1 TAT peptide binding to mimetic membranes. *Proc. Natl. Acad. Sci. USA*. 111:12684–12688.

14. Ciobanasu, C., J. P. Siebrasse, and U. Kubitscheck. 2010. Cell-Penetrating HIV1 TAT Peptides Can generates Pores in Model Membranes. *Biophys. J.* 99:153–162.

15. Ciobanasu, C., E. Harms, …, U. Kubitscheck. 2009. Cell-Penetrating HIV1 TAT Peptides Float on Model Lipid Bilayers. *Biochemistry.* 48:4728–4737.

16. Akabori, K., K. Huang, …, S. Tristram-Nagle. 2014. HIV-1 TAT membrane interaction probed using X-ray and neutron scattering, CD spectroscopy and MD simulations. *Biochim. Biophys. Acta.* 1838:3078–3087.

17. Mishra, A., V. D. Gordon, …, G. C. L. Wong. 2008. HIV TAT Forms Pores in Membranes by Inducing Saddle-Splay Curvatures: Potential Role of Bidentate Hydrogen Bonding. *Angew. Chem. Int. Ed.* 47:2986–2989.

18. Mishra, A., G. H. Lai, …, G. C. L. Wong. 2011. Translocation of HIV TAT peptide and analogues induced by multiplexed membrane and cytoskeletal interactions. *Proc. Natl. Acad. Sci. USA.* 108:16883–16888.

19. Allolio, C., A. Magarkar, …, P. Jungwirth. 2018. Arginine rich cell penetrating peptides induce membrane multilamellarity and enter via formation of a fusion pore. *Proc. Natl. Acad. Sci. USA.* 115:11923–11928.

20. Sakamoto, K., T. Morishita, …, H. Sakai. 2021. Direct entry of cell-penetrating-peptide can be controlled by maneuvering the membrane curvature. *Sci. Rep.* 11:31.

21. Garanger, E., S. R. MacEwan, …, S. Lecommandoux. 2015. Structural Evolution of a Stimulus-Responsive Diblock Polypeptide. *Macromolecules.* 48:6617–6627.

22. Maiolo, J. R., M. Ferrer, and E. A. Ottinger. 2005. Effects of cargo molecules on the cellular uptake of arginine-rich cell-penetrating peptides. *Biochim. Biophys. Acta.* 1712:161–172.

23. Zorko, M., and U. Langel. 2005. Cell-penetrating peptides: mechanism and kinetics of cargo delivery. *Adv. Drug Deliv. Rev.* 57:529–545.

24. MacEwan, S. R., and A. Chilkoti. 2012. Digital switching of local arginine density in a genetically encoded self-assembled polypeptide nanoparticle controls cellular uptake. *Nano Lett.* 12:3322–3328.

25. MacEwans, S. R., and A. Chilkoti. 2014. Applications of elastin like polypetides in drug delivery. *J. Contr. Release.* 190:314–330.

26. Sun, G., P.-Y. Hsueh, …, J. A. MacKay. 2011. Design and cellular internalization of genetically engineered polypeptide nanoparticles displaying adenovirus knob domain. *J. Contr. Release.* 155:218–226.

27. Weinberger, A., V. Walter, …, C. M. Marques. 2017. Cargo self-assembly rescues affinity of cell-penetrating peptides to lipid membranes. *Sci. Rep.* 7, 43963.

28. Meyer, D. E., G. A. Kong, …, A. Chilkoti. 2001. Targeting a Genetically Engineered Elastin-like Polypeptide to Solid Tumors by Local Hyperthermia. *Cancer Res.* 61:1548–1554.

29. MacEwan, S. R., and A. Chilkoti. 2010. Elastin-like polypeptides: Biomedical applications of tunable biopolymers. *Biopolymers.* 94:60–77.

30. Angelova, M. I., and D. S. Dimitrov. 1986. Liposome electroformation. *Faraday Discuss.* 81:303–311.

31. Perret, E., A. Leung, …, P. Nassoy. 2002. Versatile decoration of glass surfaces to probe individual protein-protein interactions and cellular adhesion. *Langmuir.* 18:846–854.

32. March, D. 2013. Handbook of Lipid Bilayers, second edition. CRC press.

33. Hill, T. L. 1988. An Introduction to Statistical Thermodynamics. Dover Pubn Inc.

34. Ziegler, A., X. L. Blatter, …, J. Seelig. 2003. Protein Transduction Domains of HIV-1 and SIV TAT Interact with Charged Lipid. *Biochemistry.* 42:9185–9194.

35. Hassouneh, W., E. B. Zhulina, …, M. Rubinstein. 2015. Elastin-like Polypetides Diblock Copolymers Self-Assemble into Weak Micelles. *Macromolecules.* 48:4183–4195.

36. May, S., D. Harries, and A. Ben-Shaul. 2000. Lipid Demixing and Protein-Protein Interactions in the adsorption of charged Proteins on Mixed Membranes. *Biophys. J.* 79:1747–1760.

37. Weinberger, A. 2013. Model Lipid Systems and Their Interactions with Polypeptides. Ph.D. thesis, University of Strasbourg.

38. Wongwailikhit, K., A. Ohta, …, M. Aratono. 2001. Temperature effect on the adsorption and micelle formation of pentaethylene glycol monoalkyl ethers. *J. Phys. Chem. B.* 105:11462–11467.

39. Hayami, Y., H. Ichikawa, …, K. Motomura. 1998. Thermodynamic study on the adsorption and micelle formation of long chain alkyltrimethylammonium chlorides. *Colloid Polym. Sci.* 276:595–600.

40. Gürses, A., S. Karaca, …, M. Açikyildiz. 2010. Monomer and micellar adsorptions of CTAB onto the clay/water interface. *Desalination.* 264:165–172.

41. Li, L., N. K. Li, …, G. P. López. 2018. Functional modification of silica through enhanced adsorption of elastin-like polypeptide block copolymers. *Biomacromolecules.* 19:298–306.